Front. Chem. Sci. Eng. 2019, 13(3): 493–500
https://doi.org/10.1007/s11705-019-1826-z

RESEARCH ARTICLE

Two-dimensional SnS_2 nanosheets on Prussian blue template for high performance sodium ion batteries

Glenn J. Sim[1,2], Kakui Ma[1], Zhixiang Huang[1], Shaozhuan Huang[1], Ye Wang[1,3], Huiying Yang (✉)[1]

1 Pillar of Engineering Product Development, Singapore University of Technology and Design, Singapore 487372, Singapore
2 Airbus Group Innovations Singapore, Singapore 797562, Singapore
3 Key Laboratory of Materials Physics of Ministry of Education, Department of Physics and Engineering, Zhengzhou University, Zhengzhou 450052, China

Abstract Three-dimensional Prussian blue (PB) nanostructures was obtained via a one-step hydrothermal method. Subsequently, two-dimensional tin disulfide (SnS_2) nanosheets were grown onto PB through a facile hydrothermal synthesis. The as prepared SnS_2/PB is further employed as the anode of sodium ion batteries (SIBs). SnS_2/PB nanoarchitecture delivers a specific capacity of 725.7 $mAh \cdot g^{-1}$ at 50 $mA \cdot g^{-1}$. When put through more than 200 cycles, it achieved a stable cycling capacity of 400 $mAh \cdot g^{-1}$ at 200 $mA \cdot g^{-1}$. The stable Na^+ storage properties of SnS_2/PB was attributed to the synergistic effect among the conductive PB carbon, used as the template in this work. These results obtained potentially paves the way for the development of excellent electrochemical performance with stable performance of SIBs.

Keywords Prussian blue, carbon nanocubes, tin disulfide, sodium ion batteries

1 Introduction

The steady rate at which fossil fuels is depleting has caused the spike of interests in renewable energy technologies [1–4]. It has attracted much interests both in the industrial and research communities as we make a conscious effort to steer away from the reliance on fossil fuels [5,6]. As the applications of renewable energy technologies in various portable electronics and electric vehicles increases, we look to a cheaper and more available source of renewable energy [7,8]. Recently, sodium-ion batteries (SIBs) have gained much attention due to its large natural abundance, which leads to the low cost of sodium salts [4,9,10]. Moreover, SIB is a suitable alternative to lithium ion battery (LIB) as it has similar insertion chemistry with lithium ions [11]. However, as the ionic radius of sodium ions (~0.106 nm) are larger as compared to lithium ions (~0.076 nm), SIBs anode materials faces a different set of challenges [12–14]. These include volume expansion, large polarization and slow reaction kinetics, which results in low reversible capacities and inferior life cycle of the battery [15,16]. Furthermore, it has also been demonstrated that the current commercial graphite-based anode materials for LIBs are not suitable to be applied in SIBs [17]. Thus, our aim to find a suitable anode material that would possess a high rate performance and long cycle life for SIBs [18].

Among these new anode materials being applied in SIBs in recent years, two-dimensional (2D) materials have been in limelight [19–21]. The large specific surface area, high electronic conductivity and low volume change during the sodiation and desodiation process attracts attention of many [22]. Tin sulfide (SnS_2) has been investigated as an anode material for SIBs due to its high theoretical capacity of 847 $mAh \cdot g^{-1}$, based on the theoretical stoichiometry of $Na_{15}Sn_4$ [23]. SnS_2 comprises of tin atoms which are sandwiched between two layers of hexagonally close packed sulfur atoms that support the intercalation of sodium as well as volume changes during alloying—dealloying reactions [24]. The weak van der Waals interaction between the SnS_2 layers makes it highly suitable to host sodium ions through a process of intercalation, conversion followed by reversible Na alloying reaction as follows [25]:

$$SnS_2 + xNa^+ + xe^- \rightarrow Na_xSnS_2 \quad (1)$$

$$Na_xSnS_2 + (4-x)Na + (4-x)e^- \rightarrow Sn + 2Na_2S \quad (2)$$

Received October 4, 2018; accepted February 8, 2019

E-mail: yanghuiying@sutd.edu.sg

$$Sn + 4.4Na^+ + e^- \leftrightarrow Na_{4.4}Sn \quad (3)$$

Wu et al. examined extensively Sn-SnS-C nanocomposites, applied as SIB anodes and reported reversible capacities of 664 and 350 $mAh \cdot g^{-1}$ at 20, 800 $mA \cdot g^{-1}$ respectively [26]. SIBs with SnO_2 as anodes (432 $mAh \cdot g^{-1}$ after 150 cycles at 20 $mA \cdot g^{-1}$) and SnO_2@graphene nanocomposite (638 $mAh \cdot g^{-1}$ after 100 cycles at 20 $mA \cdot g^{-1}$) have also been reported recently by Liu et al. [27]. They achieved an initial capacity of 722 $mAh \cdot g^{-1}$ and a capacity of 405 $mAh \cdot g^{-1}$ after 150 cycles at 50 $mA \cdot g^{-1}$ [27]. Their work consists of an array of nanorods with a carbon outer shell, a Sn sandwiched layer and a metal inner core. These progresses are encouraging, but a high capacity Sn based anode for SIB with good rate performance and long cycle life has yet to be identified [28]. The lack of cycle stability is often attributed to the deleterious volume expansion in Sn sodium alloy formation [29,30]. The expansion of 420% in volume upon the formation of $Na_{15}Sn_4$, results in electrode disintegration and gradual loss of electrical contact with the current collector due to pulverization [31,32]. SnS_2 has been synthesized with various morphologies to suppress volume changes by nanosizing which increases its surface to volume ratio as well as improve sodium kinetics by shortening the pathway for sodium ions [33,34]. SnS_2 nanostructures with nanosheet, nanobelt, nanoflower, nanoplate, and microsphere morphologies all have shown higher specific capacity and improved cycling stability as compared to bulk SnS_2 [35].

Metal-organic frameworks (MOFs) are formed by self-assembly of metal atoms and organic ligands [36]. The morphology of MOF ranges from cubic or octahedral particles to one-dimensional rods or tubes [37]. This makes it the most interesting materials. Because of the diverse morphologies, the formation of hollow structures using MOFs as templates provides endless opportunities in developing new nanomaterials which are tailorable and functional. Energy storage, energy conversion, catalysis, gas storage, gas sensing, and drug delivery are the few industries which have benefitted from the unique structures [38]. There have been several works leveraging on the templates which MOFs provide [39]. Despite all the results and progress achieved, research on the functional materials derived from MOFs is still in its infant stage [40]. Therefore, we are motivated to utilize the unique architectures which MOFs provide, to develop high-quality functional nanomaterials through facile synthesis methods [41]. Prussian blue (PB) is an example of a MOF, consisting of a mixed-valence iron (III) hexacyanoferrate (II) compound of composition $Fe_4[Fe(CN)_6]_3$ with a face-centered-cubic crystal structure [42]. $KFe_2(CN)_6$, PB, has a cubic framework with Fe(II) and Fe(III) on alternate corners of a cube of corner-shared octahedra linked by linear anions (CN^-) [43]. The low-spin Fe(III) bonds only with C atoms, the high-spin Fe(II) bonds only with N atoms, and the CN^- bond opens the faces of the elementary cubes for Na^+ to intercalate in between half-filled body-center positions [44–46].

In this work, we present a scalable synthesis of PB nanocube structures based on simple hydrothermal method. The as synthesized PB nanocubes are then etched and used as a template for SnS_2 in a hydrothermal growth. By taking advantage of the carbon network of PB microcubes, it is used a template. Benefiting from the unique structures and the coupled effects of metals and organic ligands. When evaluated as an anode material for SIBs, the as-synthesized SnS_2/PB manifested high specific capacity and excellent cycling performance. When assembled into a coin cell, SnS_2/PB showed superior sodium storage capability with high reversible capacity of ~625 $mAh \cdot g^{-1}$. The large surface area of SnS_2 provides sites for sodium ions to intercalate, leading to high capacity retention (~400 $mAh \cdot g^{-1}$ cycled at 500 $mA \cdot g^{-1}$) after hundreds of charge/discharge cycles [47].

2 Experimental

2.1 Materials

All chemicals were purchased from Sigma Aldrich and used as it is. They include: Polyvinylpyrrolidone, potassium (III) hexacyanoferrate, hydrochloric acid, tin (IV) chloride and thioacetamide.

2.2 Preparation of Prussian blue analogues (PBA)

PBA were synthesized using the following method. Polyvinylpyrrolidone (12.0 g) and potassium (III) hexacyanoferrate ($K_3Fe(CN)_6$, 0.60 g) were added to a beaker containing 200 mL of 0.1 $mol \cdot L^{-1}$ hydrochloric acid solution under magnetic stirring. After 30 min of stirring, a clear solution without any particle suspension was obtained. The beaker is then transferred into an oven for heating at 80°C for 12–18 h. The precipitates were collected by centrifugation and washed in distilled water and ethanol several times. The resulting powder was dried at 60°C to obtain PBA powders [48].

2.3 Preparation of SnS_2/PB

In a typical synthesis, 32 $mmol \cdot L^{-1}$ of tin (IV) chloride ($SnCl_4 \cdot 5H_2O$) and 80 $mmol \cdot L^{-1}$ of thioacetamide were dissolved into 35 mL ethanol. Subsequently, the as synthesized PBA powders were placed into the prepared precursor and transferred into a 50 mL Teflon-line stainless steel autoclave. The autoclave was then heated at 180°C for 16 h. After solvothermal reaction, the final product was collected by rinsing with DI water and ethanol several times and left in the drying oven at 60°C overnight [24].

2.4 Materials characterizations

Field emission scanning electron microscope (JEOL JSM-7600F) were used to study both the morphological and the energy dispersive X-ray (EDX) spectroscopy. To obtain a higher resolution microstructure analysis, studies were conducted via high resolution transmission electron microscopy (HR-TEM) and selected area electron diffraction analysis (JEOL JEM-2010, accelerating voltage of 200.0 kV). Crystal structure and phase identification were performed using X-ray diffraction techniques (XRD, Bruker D8 Advance, Cu Kα lines λ = 0.154 nm). A confocal Raman setup with a 532 nm laser excitation (WITec Instruments Corp, Germany) was used to conduct Raman spectroscopy on the samples. Thermogravimetric analysis was performed to analyze the content of all composite samples (Shimadzu DTG-60).

2.5 Coin cell assembly

The above synthesized SnS_2/PB samples were assembled into 2032 coin cell via two electrode half-cell configurations where sodium metal acts as the counter electrode. Pure PB was also prepared as a control sample. To prepare for the electrode materials, active materials were mixed with conductive carbon black and carboxymethyl cellulose (MW ≈ 700000) in ratio of 8:1:1 w/w respectively. The stated powders were mixed uniformly for at least 30 min using a mortar agate with a few drops of DI-water as solvent. The resultant slurry is coated onto Ni foam substrate and dried at 120°C for 12 h before assembly. The coin cell CR 2032 was assembled in a glove box filled with argon gas with the oxygen and moisture level lower than 1 ppm. Each coin cell consisted of a glass fiber filter (GB-100R, Advantec, Japan) membrane sandwiched between a working electrode (active material) and counter electrode (sodium metal). The sodium electrode was prepared by cutting a sodium ingot in the glove box. For the electrolyte, 1 mol of $NaPF_6$ was dissolved into ethylene carbonate/diethyl carbonates solution (1:1, v:v) with 2% fluoroethylene-carbonate as the stabilizer.

2.6 Electrochemical measurements

Electrochemical measurements were carried out on the above assembled 2032 coin cells 24 h after battery assembly. Cyclic voltammetry (CV) and electrochemical impedance spectroscopy (EIS) measurements were performed by an electrochemical workstation (VMP3, Bio-Logic, Claix, France). The galvanostatic charge and discharge test was measured in the voltage range of 0.01–3 V at various current densities ranging from 50 to 1000 $mA \cdot g^{-1}$ using a battery analyzer (Neware, Shenzhen, China).

3 Results and discussion

3.1 Characterization of PB and SnS_2/PB

The step wise synthesis process and morphology of SnS_2/PB nanostructure is presented in the illustration and the corresponding scanning electron microscopy (SEM) images in Fig. 1. In the first step, PB nanocubes were synthesized via a hydrothermal method at 80°C for 12 to 18 h. The as-prepared PB shows uniform nanocubic structure with average size of 100–200 nm in length. After etching away of Fe^{3+}, PB was placed in the teflon lined autoclave with the dissolved SnS_2 precursors for the hydrothermal growth. SnS_2 nanosheets were grown directly and uniformly onto the PB nanocubes, shown in Fig. 1(c) and Fig. S1(e). In addition, the successful growth of SnS_2 on PB can be seen from the nucleation sites in Figs. S2(a) and (b) on PB surface after 3 h in the hydrothermal reaction. The uniform growth and even loading of SnS_2 on PB can be seen after the 6th and 12th h of the hydrothermal reaction, with the consistent loading of SnS_2 on the PB increasing as the duration of the reaction increases, as seen in Figs. S2(c) and S2(e). The high magnification SEM images seen in Figs. S2(b), S1(d) and S1(f) also show the gradual increase of the growth of SnS_2 on PB as the teflon lined autoclave was left in the oven for an increased period [49].

The detailed morphology of SnS_2 and pristine PB was shown in the TEM images as shown in Figs. 2(a–d). Figure 2(a) further proves the uniform growth of SnS_2 on the PB nanocubes. From Fig. 2(a), fine sheets of SnS_2 can be clearly observed on the PB. In the HR-TEM image in Fig. 2(b), the interplanar spacing of 5.9 Å can be assigned to the (001) crystal planes of SnS_2 [50]. Figure 2(c) shows a low magnification TEM image of another segment from the

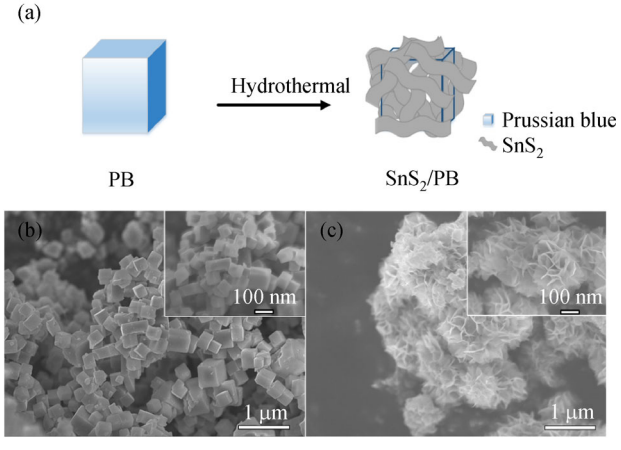

Fig. 1 (a) Illustration of the growth process of PB and (b) SnS_2/PB via hydrothermal method. Low and high (inset) magnification of SEM images of (c) PB and (d) SnS_2/PB

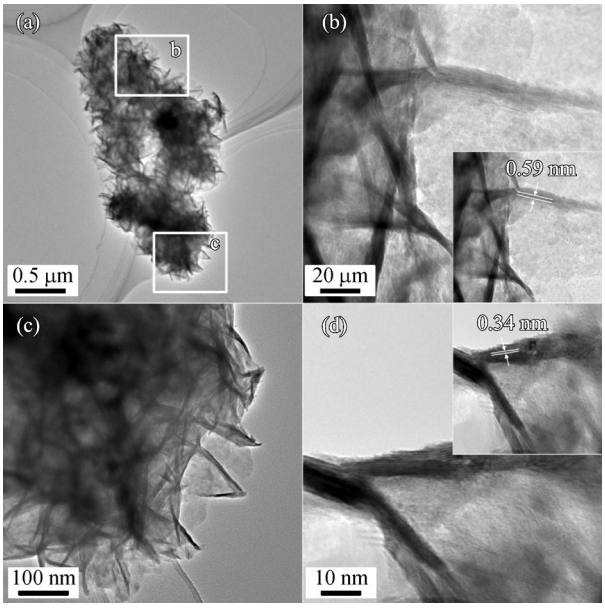

Fig. 2 HRTEM images of (a) low magnification of SnS_2/PB, (b) high magnification of SnS_2/PB showing (c) low magnification of SnS_2/PB, and (d) enlarged regions of SnS_2/PB showing lattice of SnS_2 in the 002 plane

sample in Fig. 2(a). The HR-TEM image in Fig. 2(d) exhibits the interplanar spacing of 3.4 Å can be assigned to the (002) crystal planes of SnS_2 [51].

In addition, EDX spectroscopy analysis in Fig. S1 shows homogenously distributed elements, Sn and S, which implies the uniform growth of SnS_2 on the surfaces of PB, and the mapping spectrum in Fig. S1 of the image in Fig. S1(a) (inset) shows the decomposition of Sn and S. The ratio of Sn to S atom is close to 1:2, corresponding to the of composition of SnS_2. The crystalline phase and structure of the as-synthesized PB and SnS_2/PB nanoarchitectures were performed via XRD as shown in Fig. S3. The intense peaks located at 17.0°, 24.5°, 34.8°, 38.0°, 51.3°, 53.8°, and 56.9°, which can be well indexed to the (200), (220), (400), (420), (440), (600) and (620) cubic PB analogous (JCPDS No. 73-0687). After etching in 0.1 $mol \cdot L^{-1}$ HCl and a facile hydrothermal growth of SnS_2, the new major intense peaks located at 15.0°, 28.2°, 32.0°, 41.9°, 50.0° and 52.4°, which can be well indexed to the (001), (101), (102), (110), (111) and (201) planes of hexagonal SnS_2 (JCPDS No.23-0677), respectively [52,53].

3.2 Sodium ion electrochemical performance

The electrochemical properties of SnS_2/PB are evaluated via electrochemical characterization through CV and galvanostatic charge-discharge cycling. These electrochemical tests were conducted using coin cells with sodium metal as the counter electrode. The control sample of PB was tested in the exact same conditions. Figures 3(a) and 3 (b) show the charge and discharge curves during cycling in the CV curves of the SnS_2/PB and PB electrodes, respectively. The cells were scanned at voltages in the range 0.001–3.0 V, with a scan rate of 0.1 $mV \cdot s^{-1}$ [54].

The sodium ion storage behavior of SnS_2/PB was first characterized by CV as shown in Fig. 3(a). The CV curves of the SnS_2/PB electrode for the first cathodic sweep shows three cathodic peaks at 1.4 V, 0.7 V and 0.02 V. The cathodic peak at 1.4 V is ascribed to the intercalation of Na^+ ions into SnS_2 layers without composition change, forming Na_xSnS_2. The cathodic peak at 0.7 V reveals the following conversion reaction between sodium ions and Na_xSnS_2, in which metallic Sn and Na_2S are formed [55]. A sloping curve is observed at a lower voltage, which is indicative of the alloying reaction between sodium ions and Sn. The cathodic peak at 0.2 V arises from the formation of gel-like solid electrolyte-interface (SEI) film at the interface of the active materials and electrolyte as it is disappeared in the following cycles [56]. In the first anodic sweep, two broad oxidation peaks were observed at 0.5 V and 1.7 V in the first charging process, which corresponded to the oxidation of the Sn nanosheets to SnS_2. The effect of nanosheets of SnS_2 grown on PB templates are verified in the peak at 1.7 V. After the first cycle, the reduction peak at 0.2 V disappeared and the second and third discharging/charging curves are overlapping. This suggests high reversibility and cycling stability of Na^+ storage in the SnS_2/PB composite layer. The CV curve of PB electrode is almost same as that of SnS_2/PB electrode but with peak slightly shift (Fig. 3(b)).

The rate capability of the anode material is an important performance indicator for grid scale electricity storage and other mobile electronic devices applications. The rate capabilities of both SnS_2/PB and PB electrodes were measured at various current densities as shown in Fig. 4(a). The PB electrode was able to deliver reversible charge-discharge capacities of 183.9, 162.2, 146.6, 132.1 and 123.6 $mAh \cdot g^{-1}$ at current densities of 50, 100, 200, 500 and 1000 $mA \cdot g^{-1}$ respectively. Owing to the increased sites for sodiation due to the facile hydrothermal growth of SnS_2 on the PB templates, the SnS_2/ PB electrode was able to deliver significantly higher discharge capacities. The SnS_2/PB electrode delivered reversible charge-discharge capacities of 725.7, 509.6, 410.5, 319.6, and 195.2 $mAh \cdot g^{-1}$ at current densities of 50, 100, 200, 500 and 1000 $mA \cdot g^{-1}$ respectively. Furthermore, the capacity was restored back to 723.6 $mAh \cdot g^{-1}$ when the electrode was cycled back to the current density of 50 $mA \cdot g^{-1}$. This further proves the stability and cyclability of SnS_2/PB. The high rate performance in SnS_2/PB could be attributed to PB lowering the energy barrier for Na^+ ion insertion, coupled with the morphology of the anchored PB templates, which creates a short diffusion pathway for the exchange of sodium ions and electrons from the SnS_2 nanoparticles

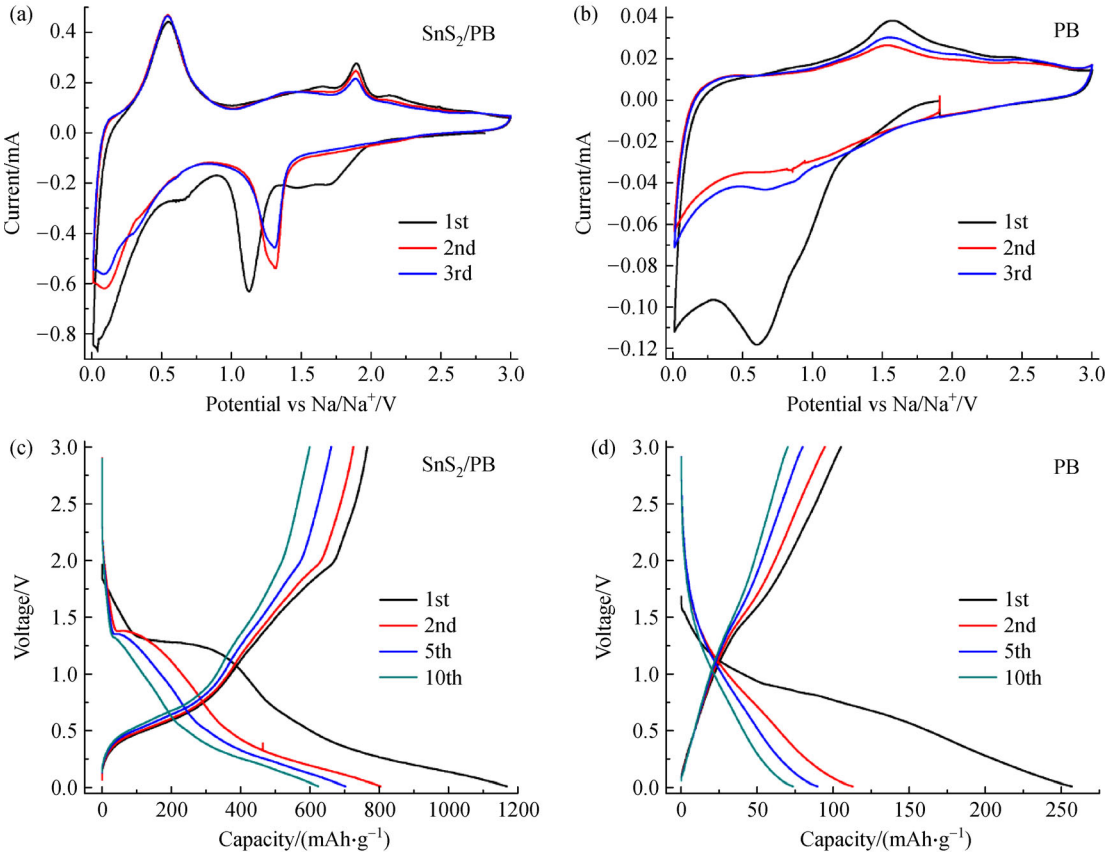

Fig. 3 Cyclic voltammograms of (a) SnS_2/PB electrode and (b) PB electrode at a rate of 0.05 $mV \cdot s^{-1}$ in a potential range of 0.01 to 3.0 V. Galvanostatic discharge and charge curves of (c) SnS_2/PB and (d) PB electrodes in the potential range of 0.01 to 3.0 V

through the well-connected network [57]. PB serves as a good conductive network and a substrate, having negligible capacity as seen in Fig. 3(d) [58]. Thus, the overall capacity can be attributed completely to the SnS_2 nanosheets grown on the PB template.

The cycling stability of SnS_2/PB and PB electrodes were measured at a current density of 50 $mA \cdot g^{-1}$ for the first 5 cycles for the activation process, followed by measuring at 500 $mA \cdot g^{-1}$ up to 200 cycles. This can be seen in Fig. 4(b). Highly reversible and stable cycling was also observed for the SnS_2/PB electrode with a capacity retention is 98% after 200 cycles (compared from the 6th cycle onwards), shown in Fig. 4(b). The SnS_2/PB electrode maintained a capacity of about 400 $mAh \cdot g^{-1}$ throughout the 200 cycles, while the PB electrode maintained a capacity of about 200 $mAh \cdot g^{-1}$ throughout the 200 cycles, corresponding to the rate capability curve (Fig. 4(a)). Furthermore, the initial coulombic efficiency is also consistent with that at 50 $mA \cdot g^{-1}$ of 76.5%, which increased and maintain near 100% in subsequent cycles. This high capacity, highly reversible and stable cycling implies the improved electrochemical performance in sodium storage of SnS_2 is attributed to the large surface area of SnS_2 which results from the hydrothermal growth of SnS_2 on the PB template.

EIS measurements were conducted for both to investigate the intrinsic electrochemical kinetics of these two electrodes. The measurements were performed on the coin cells at a semi-charged state (~2.5 V) across a frequency range of 10 mHz to 1 MHz as shown in Fig. 5. The Nyquist diagram were fitted using the circuitry model as shown in the inset of Fig. 5(b), where R_s represents the is resistance of both the current collector and electrolyte; R_f and Q_1 represent the resistance of the SEI layer and constant phase element respectively; R_{ct} and Q_2 represent the resistance of the charge transfer and double layer capacitor respectively. Z_w represents the Warburg impedance, which is related to the sodium diffusion in the coin cell. As seen in the Fig. 5(a), curves from both SnS_2/PB and PB electrodes display a similar profile. They have a small semi-circle in the high frequency region followed by an acute straight line in the low frequency region. The semi-circle region corresponds to a combination of resistance in the surface film and resistance of the charge transfer. The acute straight line arises from the Warburg region as well as sodium accumulation element. The fitted values using the equivalent circuit are presented in Table 1. The results

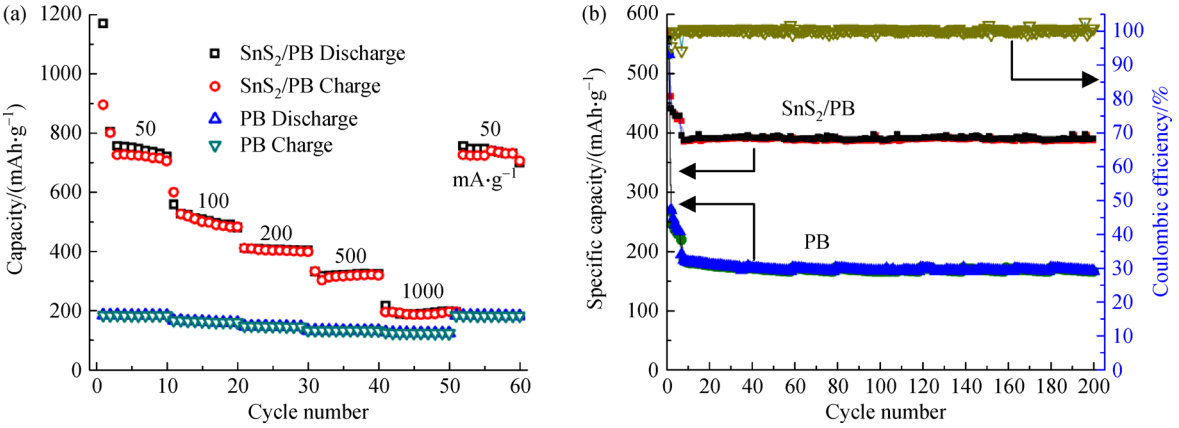

Fig. 4 (a) Rate capability of SnS_2/PB and PB electrodes; (b) long cycling performance of SnS_2/PB and PB electrodes at a current density of 500 mA·g^{-1}, and the corresponding coulombic efficiency of SnS_2/PB electrode. The first 5 cycles were cycled at current density of 50 mA·g^{-1} for activation of the cell

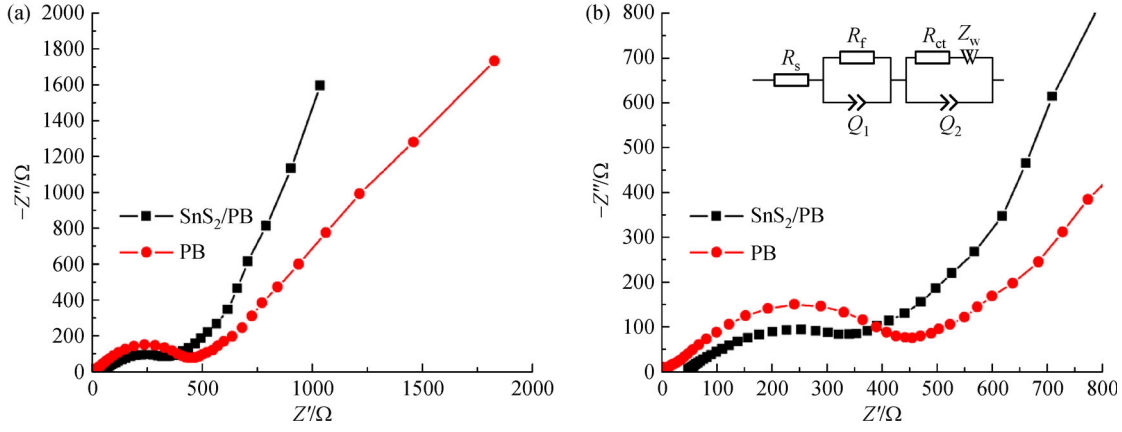

Fig. 5 Nyquist impedance spectra of SnS_2/PB and PB electrodes. (a) In the full range of Z' from 0 to 2000 Ω; (b) enlarged in the region of $-Z''$ from 0 to 800 Ω, with the inset showing the model of the EIS circuit

show that with the hydrothermal growth of SnS_2 onto the surface of the PB, the charge transfer resistance of the SnS_2/PB electrodes (98.0 Ω) is significantly less than that of the PB electrodes (157.0 Ω). It is therefore evident that the SnS_2/PB electrodes possesses better electrical conductivity and faster charge-transfer reaction for the sodium ion and electrons. This stable impedance demonstrates the robustness of the stable SEI layer and the robust structural integrity during charge-discharge cycles.

Table 1 Fitting results of the EIS spectra using the equivalent circuit shown in Fig. 4(b)

Sample	R_s /Ω	R_f /Ω	R_{ct} /Ω
SnS_2/PB	3.8	598.2	98.0
PB	4.6	410.8	157.0

4 Conclusions

In summary, SnS_2/PB anode material was synthesized via two steps. First, PB nanocubes were derived from a simple hydrothermal synthesis. After etching, the PB nanocubes were used as a template for the next step. SnS_2 nanosheets were grown on the PB nanocubes, giving rise SnS_2/PB hybrid nanoarchitecture. The SnS_2/PB nanoarchitecture exhibits high capacity, long cycle life and exceptional rate capabilities as an anode of SIBs. In specific, it delivers a capacity of 725.7 mAh·g^{-1} at 50 mA·g^{-1}. When cycled through 200 cycles, it achieved a stable cycling capacity of 400 mAh·g^{-1} at 200 mA·g^{-1}. Such excellent electrochemical performance is attributed to the synergistic effect between SnS_2 and PB. This enhanced SIB performance further proves that SnS_2 has the capabilities and potential as an anode material for SIBs.

Acknowledgements This research work is supported by Singapore University of Technology and Design DmanD center.

Electronic Supplementary Material Supplementary material is available in the online version of this article at https://doi.org/10.1007/s11705-019-1826-z and is accessible for authorized users.

References

1. Tarascon J M, Armand M. Issues and challenges facing rechargeable lithium batteries. Nature, 2001, 414(6861): 359–367
2. Dunn B, Kamath H, Tarascon J M. Electrical energy storage for the grid: A battery of choices. Science, 2011, 334(6058): 928–935
3. Armand M, Tarascon J M. Building better batteries. Nature, 2008, 451: 652–657
4. Slater M D, Kim D, Lee E, Johnson C S. Sodium ion batteries. Advanced Functional Materials, 2013, 23: 947–958
5. Wang Q, Jiang B, Li B, Yan Y. A critical review of thermal management models and solutions of lithium-ion batteries for the development of pure electric vehicles. Renewable & Sustainable Energy Reviews, 2016, 64: 106−128
6. Liserre M, Sauter T, Hung J Y. Future energy systems: Integrating renewable energy sources into the smart power grid through industrial electronics. IEEE Industrial Electronics Magazine, 2010, 4(1): 18–37
7. Pan H, Hu Y S, Chen L. Room-temperature stationary sodium-ion batteries for large-scale electric energy storage. Energy & Environmental Science, 2013, 6(8): 2338–2360
8. Ellabban O, Abu-Rub H, Blaabjerg F. Renewable energy resources: Current status, future prospects and their enabling technology. Renewable & Sustainable Energy Reviews, 2014, 39: 748–764
9. Cao Y, Xiao L, Sushko M L, Wang W, Schwenzer B, Xiao J, Nie Z, Saraf L V, Yang Z, Liu J. Sodium ion insertion in hollow carbon nanowires for battery applications. Nano Letters, 2012, 12(7): 3783–3787
10. Kundu D, Talaie E, Duffort V, Nazar L F. The emerging chemistry of sodium ion batteries for electrochemical energy storage. Angewandte Chemie International Edition, 2015, 54(11): 3431–3448
11. Wang Y, Xing G, Han Z J, Shi Y, Wong J I, Huang Z X, Ostrikov K K, Yang H Y. Pre-lithiation of onion-like carbon/MoS_2 nano-urchin anodes for high-performance rechargeable lithium ion batteries. Nanoscale, 2014, 6(15): 8884–8890
12. Yabuuchi N, Kubota K, Dahbi M, Komaba S. Research development on sodium-ion batteries. Chemical Reviews, 2014, 114(23): 11636–11682
13. Balogun M S, Luo Y, Qiu W, Liu P, Tong Y. A review of carbon materials and their composites with alloy metals for sodium ion battery anodes. Carbon, 2016, 98(Supplement C): 162–178
14. Wang L, Lu Y, Liu J, Xu M, Cheng J, Zhang D, Goodenough J B. A superior low-cost cathode for a Na-ion battery. Angewandte Chemie International Edition, 2013, 52(7): 1964–1967
15. Deng W, Liang X, Wu X, Qian J, Cao Y, Ai X, Feng J, Yang H. A low cost, all-organic Na-ion battery based on polymeric cathode and anode. Scientific Reports, 2013, 3: 2671
16. Jache B, Adelhelm P. Use of graphite as a highly reversible electrode with superior cycle life for sodium-ion batteries by making use of co-intercalation phenomena. Angewandte Chemie International Edition, 2014, 53(38): 10169–10173
17. Lin D, Liu Y, Cui Y. Reviving the lithium metal anode for high-energy batteries. Nature Nanotechnology, 2017, 12(3): 194
18. Bommier C, Luo W, Gao W Y, Greaney A, Ma S, Ji X. Predicting capacity of hard carbon anodes in sodium-ion batteries using porosity measurements. Carbon, 2014, 76(Supplement C): 165–174
19. Yan C, Lv C, Zhu Y, Chen G, Sun J, Yu G. Engineering 2D nanofluidic Li-ion transport channels for superior electrochemical energy storage. Advanced Materials, 2017, 29(46): 1703909
20. Wu Y, Nie P, Wu L, Dou H, Zhang X. 2D MXene/SnS_2 composites as high-performance anodes for sodium ion batteries. Chemical Engineering Journal, 2018, 334: 932–938
21. Wang X, Kajiyama S, Iinuma H, Hosono E, Oro S, Moriguchi I, Okubo M, Yamada A. Pseudocapacitance of MXene nanosheets for high-power sodium-ion hybrid capacitors. Nature Communications, 2015, 6: 6544
22. Seo J W. Jang J T, Park S W, Kim C, Park B, Cheon J. Two-dimensional SnS_2 nanoplates with extraordinary high discharge capacity for lithium ion batteries. Advanced Materials, 2008, 20 (22): 4269–4273
23. Zai J, Wang K, Su Y, Qian X, Chen J. High stability and superior rate capability of three-dimensional hierarchical SnS_2 microspheres as anode material in lithium ion batteries. Journal of Power Sources, 2011, 196(7): 3650–3654
24. Huang Z X, Wang Y, Wong J I, Yang H Y. Free standing SnS_2 nanosheets on 3D graphene foam: An outstanding hybrid nanostructure anode for Li-ion batteries. 2D Materials, 2015, 2(2): 024010
25. Qu B, Ma C, Ji G, Xu C, Xu J, Meng Y S, Wang T, Lee J Y. Layered SnS_2-reduced graphene oxide composite—a high-capacity, high-rate, and long-cycle life sodium-ion battery anode material. Advanced Materials, 2014, 26(23): 3854–3859
26. Wu L, Hu X, Qian J, Pei F, Wu F, Mao R, Ai X, Yang H, Cao Y. A Sn-SnS-C nanocomposite as anode host materials for Na-ion batteries. Journal of Materials Chemistry. A, Materials for Energy and Sustainability, 2013, 1(24): 7181–7184
27. Liu Y, Fang X, Ge M, Rong J, Shen C, Zhang A, Enaya H A, Zhou C. SnO_2 coated carbon cloth with surface modification as Na-ion battery anode. Nano Energy, 2015, 16: 399–407
28. Wu L, Hu X, Qian J, Pei F, Wu F, Mao R, Ai X, Yang H, Cao Y. Sb-C nanofibers with long cycle life as an anode material for high-performance sodium-ion batteries. Energy & Environmental Science, 2014, 7(1): 323–328
29. Xiao L, Cao Y, Xiao J, Wang W, Kovarik L, Nie Z, Liu J. High capacity, reversible alloying reactions in SnSb/C nanocomposites for Na-ion battery applications. Chemical Communications, 2012, 48(27): 3321–3323
30. Prikhodchenko P V, Denis Y, Batabyal S K, Uvarov V, Gun J, Sladkevich S, Mikhaylov A A, Medvedev A G, Lev O. Nanocrystalline tin disulfide coating of reduced graphene oxide produced by the peroxostannate deposition route for sodium ion battery anodes. Journal of Materials Chemistry. A, Materials for Energy and Sustainability, 2014, 2(22): 8431–8437

31. Liu Y, Zhang N, Jiao L, Tao Z, Chen J. Ultrasmall Sn nanoparticles embedded in carbon as high-performance anode for sodium-ion batteries. Advanced Functional Materials, 2015, 25(2): 214–220
32. Xu W, Zhao K, Zhang L, Xie Z, Cai Z, Wang Y. SnS_2@graphene nanosheet arrays grown on carbon cloth as freestanding binder-free flexible anodes for advanced sodium batteries. Journal of Alloys and Compounds, 2016, 654: 357–362
33. Zhu H, Jia Z, Chen Y, Weadock N, Wan J, Vaaland O, Han X, Li T, Hu L. Tin anode for sodium-ion batteries using natural wood fiber as a mechanical buffer and electrolyte reservoir. Nano Letters, 2013, 13 (7): 3093–3100
34. Xiong X, Yang C, Wang G, Lin Y, Ou X, Wang J H, Zhao B, Liu M, Lin Z, Huang K. SnS nanoparticles electrostatically anchored on three-dimensional *N*-doped graphene as an active and durable anode for sodium-ion batteries. Energy & Environmental Science, 2017, 10(8): 1757–1763
35. Chao D, Zhu C, Yang P, Xia X, Liu J, Wang J, Fan X, Savilov S V, Lin J, Fan H J. Array of nanosheets render ultrafast and high-capacity Na-ion storage by tunable pseudocapacitance. Nature Communications, 2016, 7: 12122
36. Ren W, Zhang H, Guan C, Cheng C. Ultrathin MoS_2 nanosheets@ metal organic framework-derived *N*-doped carbon nanowall arrays as sodium ion battery anode with superior cycling life and rate capability. Advanced Functional Materials, 2017, 27(32): 1702116
37. Li Q, Xu P, Gao W, Ma S, Zhang G, Cao R, Cho J, Wang H L, Wu G. Graphene/graphene-tube nanocomposites templated from cage-containing metal-organic frameworks for oxygen reduction in Li-O_2 batteries. Advanced Materials, 2014, 26(9): 1378–1386
38. Kreno L E, Leong K, Farha O K, Allendorf M, Van Duyne R P, Hupp J T. Metal-organic framework materials as chemical sensors. Chemical Reviews, 2011, 112(2): 1105–1125
39. Rowsell J L, Yaghi O M. Metal-organic frameworks: A new class of porous materials. Microporous and Mesoporous Materials, 2004, 73 (1-2): 3–14
40. James S L. Metal-organic frameworks. Chemical Society Reviews, 2003, 32(5): 276–288
41. Huang G, Zhang F, Du X, Qin Y, Yin D, Wang L. Metal organic frameworks route to *in situ* insertion of multiwalled carbon nanotubes in Co_3O_4 polyhedra as anode materials for lithium-ion batteries. ACS Nano, 2015, 9(2): 1592–1599
42. Neff V D. Some performance characteristics of a prussian blue battery. Journal of the Electrochemical Society, 1985, 132: 1382–1384
43. Lu Y, Wang L, Cheng J, Goodenough J B. Prussian blue: A new framework of electrode materials for sodium batteries. Chemical Communications, 2012, 48(52): 6544–6546
44. You Y, Wu X L, Yin Y X, Guo Y G. High-quality prussian blue crystals as superior cathode materials for room-temperature sodium-ion batteries. Energy & Environmental Science, 2014, 7(5): 1643–1647
45. Zhang Y, Wen Y, Liu Y, Li D, Li J. Functionalization of single-walled carbon nanotubes with prussian blue. Electrochemistry Communications, 2004, 6(11): 1180–1184
46. Jiang Y, Yu S, Wang B, Li Y, Sun W, Lu Y, Yan M, Song B, Dou S. Prussian blue@C composite as an ultrahigh-rate and long-life sodium-ion battery cathode. Advanced Functional Materials, 2016, 26(29): 5315–5321
47. Jiang Y, Wei M, Feng J, Ma Y, Xiong S. Enhancing the cycling stability of Na-ion batteries by bonding SnS_2 ultrafine nanocrystals on amino-functionalized graphene hybrid nanosheets. Energy & Environmental Science, 2016, 9(4): 1430–1438
48. Lim Y V, Huang S, Zhang Y, Kong D, Wang Y, Guo L, Zhang J, Shi Y, Chen T P, Ang L K. Bifunctional porous iron phosphide/carbon nanostructure enabled high-performance sodium-ion battery and hydrogen evolution reaction. Energy Storage Materials, 2018, 15: 98–107
49. Zhai C, Du N, Yang H Z D. Large-scale synthesis of ultrathin hexagonal tin disulfide nanosheets with highly reversible lithium storage. Chemical Communications, 2011, 47(4): 1270–1272
50. Ma J, Lei D, Mei L, Duan X, Li Q, Wang T, Zheng W. Plate-like SnS_2 nanostructures: Hydrothermal preparation, growth mechanism and excellent electrochemical properties. CrystEngComm, 2012, 14 (3): 832–836
51. Kim T J, Kim C, Son D, Choi M, Park B. Novel SnS_2-nanosheet anodes for lithium-ion batteries. Journal of Power Sources, 2007, 167(2): 529–535
52. Mukaibo H, Yoshizawa A, Momma T, Osaka T. Particle size and performance of SnS_2 anodes for rechargeable lithium batteries. Journal of Power Sources, 2003, 119: 60–63
53. Luo B, Fang Y, Wang B, Zhou J, Song H, Zhi L. Two dimensional graphene-SnS_2 hybrids with superior rate capability for lithium ion storage. Energy & Environmental Science, 2012, 5(1): 5226–5230
54. Yue Y, Binder A J, Guo B, Zhang Z, Qiao Z A, Tian C, Dai S. Mesoporous prussian blue analogues: Template-free synthesis and sodium-ion battery applications. Angewandte Chemie International Edition, 2014, 53(12): 3134–3137
55. Liu Y, Kang H, Jiao L, Chen C, Cao K, Wang Y, Yuan H. Exfoliated-SnS_2 restacked on graphene as a high-capacity, high-rate, and long-cycle life anode for sodium ion batteries. Nanoscale, 2015, 7(4): 1325–1332
56. Zhang Y, Zhu P, Huang L, Xie J, Zhang S, Cao G, Zhao X. Few-layered SnS_2 on few-layered reduced graphene oxide as Na-ion battery anode with ultralong cycle life and superior rate capability. Advanced Functional Materials, 2015, 25(3): 481–489
57. Yang D, Xu J, Liao X Z, He Y S, Liu H, Ma Z F. Structure optimization of prussian blue analogue cathode materials for advanced sodium ion batteries. Chemical Communications, 2014, 50(87): 13377–13380
58. Nie P, Yuan J, Wang J, Le Z, Xu G, Hao L, Pang G, Wu Y, Dou H, Yan X. Prussian blue analogue with fast kinetics through electronic coupling for sodium ion batteries. ACS Applied Materials & Interfaces, 2017, 9(24): 20306–20312